APPLIED SCIENCES AND ENGINEERING

3D printed personalized magnetic micromachines from patient blood–derived biomaterials

Hakan Ceylan[1†], Nihal Olcay Dogan[1,2†], Immihan Ceren Yasa[1], Mirac Nur Musaoglu[1,3], Zeynep Umut Kulali[1,3], Metin Sitti[1,2,3]*

Copyright © 2021 The Authors, some rights reserved; exclusive licensee American Association for the Advancement of Science. No claim to original U.S. Government Works. Distributed under a Creative Commons Attribution License 4.0 (CC BY).

While recent wireless micromachines have shown increasing potential for medical use, their potential safety risks concerning biocompatibility need to be mitigated. They are typically constructed from materials that are not intrinsically compatible with physiological environments. Here, we propose a personalized approach by using patient blood–derivable biomaterials as the main construction fabric of wireless medical micromachines to alleviate safety risks from biocompatibility. We demonstrate 3D printed multiresponsive microswimmers and microrollers made from magnetic nanocomposites of blood plasma, serum albumin protein, and platelet lysate. These micromachines respond to time-variant magnetic fields for torque-driven steerable motion and exhibit multiple cycles of pH-responsive two-way shape memory behavior for controlled cargo delivery and release applications. Their proteinaceous fabrics enable enzymatic degradability with proteinases, thereby lowering risks of long-term toxicity. The personalized micromachine fabrication strategy we conceptualize here can affect various future medical robots and devices made of autologous biomaterials to improve biocompatibility and smart functionality.

INTRODUCTION

Mobile wireless micromachines proliferate with a diverse design range and functional versatility, enabling previously unknown approaches in minimally invasive and targeted therapies in medicine (*1*–*4*). Despite the recent advances in their design (*5*, *6*), fabrication (*7*, *8*), and remote control strategies (*9*, *10*), interaction dynamics of micromachines with local live microenvironments are usually overlooked. Deployment of such micromachines in the body for extended durations can pose substantial safety risks from their biocompatibility, since any synthetic material that enters or stays inside the body is actively nonbiocompatible, and the body will counteract to eliminate it (*11*). The elimination mechanism depends on the type of construction materials, the engineering design and exposure time, and the local conditions of the biological environment, which define the complex interaction dynamics for the activation of defense cascades. The body can respond, for example, by forming a fibrotic tissue around an implant material using fibroblast activity (*11*) or engulfing micro- or nanoparticles through macrophage activity (*12*). We have recently shown that the morphological design parameters can notably affect the interaction dynamics with the cells of both primary and secondary lines of the immune system (*13*).

In addition to optimizing the structural and morphological design, other efforts have focused on the material compositions of construction to improve the biocompatibility of small-scale mobile machines by minimizing unintended interactions with the live environment. To this end, initially, matrix polymers, such as polyethylene glycol (PEG)–based materials, were explored. They provide nanoparticles and molecular drugs with stealth protection by extending their circulation time (*14*). Nevertheless, in the following years, it was realized that cosmetics-related overuse of PEG-based polymers resulted in the development of anti-PEG antibodies in a considerable part of the human population, thereby lowering the potential of PEGs in medical robots and devices (*15*). Zwitterionic polymers, which create a high-degree ion-induced hydration barrier, were considered an alternative to PEG (*16*). However, the success of these materials in the clinical application remains elusive, as there are examples where such materials can also raise antibodies within the body (*17*). In search of alternative design strategies, surface coating of microswimmers with the red blood cell membrane also proved a viable strategy; however, the stability of this supramolecular coating in live environments is not evident (*18*). In these constructs, once the coating is worn off, the nonbiocompatible interior core needs further attention. Our group and others have explored the potential of naturally derived biodegradable polymers, such as gelatin derivatives, as the dispersive matrix of medical microrobots (*19*–*21*). Concerning biocompatibility, however, materials originating from animal or plant sources can also cause serious hypersensitivity reactions in susceptible people (*22*). As a result, there is room to explore medical robots and device materials to minimize interactions with the surrounding live environment.

Here, we propose a personalized approach by using patient blood–derivable biomacromolecules in the fabrication of micromachines. Patient-derivable autologous biomaterials can minimize any risk of cytotoxicity and immune responses as the body would recognize them as self (*23*). Their proteinaceous fabrics can enable enzymatic degradability, thereby lowering risks of chronic long-term toxicity. Furthermore, they can eliminate the risk of disease transmission and lower hurdles from potential medical device regulations when these micromachines come to the stage of clinical testing (*24*).

We demonstrate the feasibility of three-dimensionally (3D) printed multiresponsive magnetic microswimmers and microrollers from blood-harvested plasma, albumin, and platelet lysate. Without introducing any further chemical reactive sites in these biomaterials, we describe the preparation of magnetic nanocomposites as the precursors of two-photon polymerization-based 3D printing. Magnetic micromachines respond to time-variant magnetic fields for both torque-driven rotational motion and steering and exhibit two-way shape memory behavior for controlled pH- and enzyme-responsive

[1]Physical Intelligence Department, Max Planck Institute for Intelligent Systems, 70569 Stuttgart, Germany. [2]Institute for Biomedical Engineering, ETH Zürich, 8092 Zürich, Switzerland. [3]School of Medicine and College of Engineering, Koç University, 34450 Istanbul, Turkey.
*Corresponding author. Email: sitti@is.mpg.de
†These authors contributted equally to this work as first authors.

Downloaded from https://www.science.org on November 24, 2021

cargo release applications. The personalized micromachine fabrication strategy we conceptualize here can affect the design of various future medical robots and devices made of autologous biomaterials for their improved biocompatibility and intelligent functionality.

RESULTS AND DISCUSSION

Concept and the fabrication process of personalized micromachines

From the practical point of view, any patient-derivable biomaterial to fabricate personalized robots should be abundantly available for harvesting in the human body. It should be easy to harvest without causing notable patient discomfort. It should be conveniently adaptable to robot fabrication. In compliance with these factors, we selected blood as a feasible patient-derivable robotic material. An average adult can donate up to around half a liter of their blood without compromising healthy body functioning. Blood is suitable for further processing. The collected whole blood can be conveniently separated into various components—such as plasma, red blood cells, and platelets—using the traditional density gradient centrifugation (Fig. 1). Plasma, which accounts for 55% of the harvested whole blood volume, can be further processed to isolate individual biomacromolecules, such as albumin, which is the most abundant protein in plasma [ca. 10 weight % (wt %)]. Platelet-based hydrogels are being explored as powerful 3D cell culture platforms for tissue engineering, as they are rich in growth factors, cytokines, and other proteins (*25*). Considering all these advantages, here, we focused on the following blood components: (i) plasma, (ii) blood albumin, and (iii) platelet lysate for the fabrication of micromachines.

We used two-photon polymerization-based 3D printing, alternatively known as two-photon direct laser writing, to fabricate various medical micromachines with intricate morphological and compositional features (*26*). This 3D printing technique has been increasingly used in the microrobotics community in recent years, as it can enable complex 3D machine morphologies and various functional material compositions with down to 100-nm fabrication resolution (*8*). This technique relies on the simultaneous absorption of two half-energy photons by the photoinitiator in a fraction of the focal volume of a femtosecond-pulsed infrared laser. The spatial control of the two-photon absorption enables highly complex 3D computer-aided designs (CADs) with submicron features and the introduction of diverse chemical functionalities (*7*, *27*).

We fabricated micromachines from the above blood-harvested materials by forming a precursor mixture with a rose bengal and magnetic iron oxide nanoparticles. Rose bengal served as the photosensitizer, leading to direct photocrosslinking of the biomacromolecules as harvested in their raw forms (fig. S1) (*28*–*30*). As a result, we did not have to modify the molecular composition of the biomacromolecules to not introduce potentially toxic and immunogenic acrylate or methacrylate groups (*31*). Rose bengal is also a nontoxic molecule that is clinically demonstrated as a photochemical tissue glue (*32*, *33*). Iron oxide nanoparticles served as magnetic transducers to create externally powered propulsion. A clean and aggregate-free aqueous mixture was of paramount importance for 3D printing of high-fidelity micromachines with submicron features. We applied this fabrication approach on the following most common and promising medical micromachine designs at microscopic length scales: single-helix microswimmer (*34*, *35*), double-helix microswimmer (*20*, *36*), and microroller (*37*, *38*).

3D printed micromachines

The laser intensity during the 3D printing is one of the most critical parameters tuned for each design and precursor solution to obtain high-quality microstructures. To this end, we first optimized the laser intensity for albumin micromachines. We generated a double-helix microswimmer array printed with varying laser intensities in the range of 7.78×10^{13} to 1.21×10^{14} W cm^{-2} (Fig. 2, A and B). The micromachines printed with stepwise changed laser intensities resulted in different structural qualities, categorized as underdose, acceptable dose, and overdose (Fig. 2, B and C). This categorization was applied on the basis of the structural fidelity and the basic dimension measurements of the micromachines, i.e., length, compared to the original CAD (Fig. 2C and table S1). The micromachines printed with insufficient laser intensity failed to establish adequate crosslinking density and could not match the original design. The micromachines fabricated with excessive laser intensity became bigger than the design due to the excessive propagation of the two-photon polymerization. At even higher doses, the micromachines exhibited

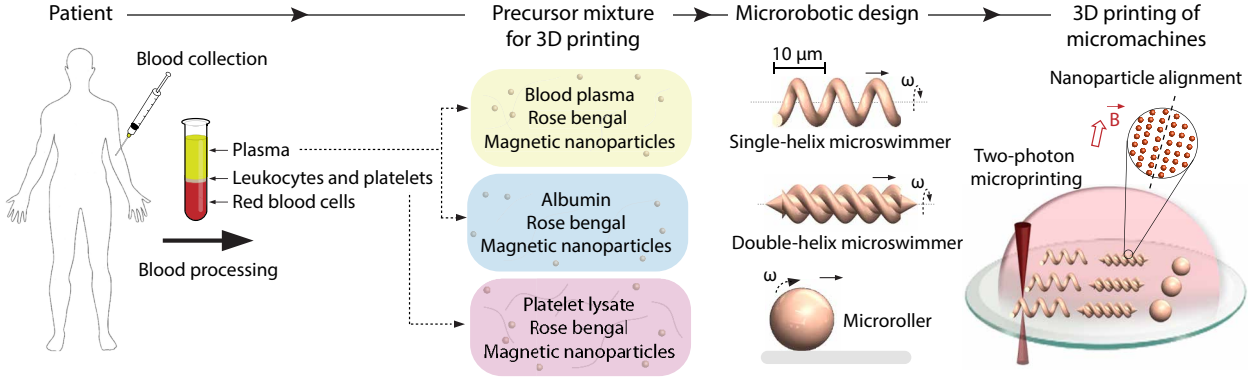

Fig. 1. A facile strategy for the 3D printed personalized micromachines from patient blood–derivable biomaterials. Harvested blood from the patient can be rapidly and robustly processed to obtain blood plasma, albumin, and platelet lysate. We use these biomacromolecules to prepare the microfabrication precursor mixtures containing the photosensitizer rose bengal and magnetic iron oxide nanoparticles for wireless powering and control. CADs of the micromachines are then realized by two-photon polymerization-based 3D printing. During the 3D printing process, we apply a uniform magnetic $\vec{B}$ field in the direction perpendicular to the rotation axis of the micromachines to maximize the net magnetization by self-assembling the magnetic nanoparticles into directional chains.

Downloaded from https://www.science.org on November 24, 2021

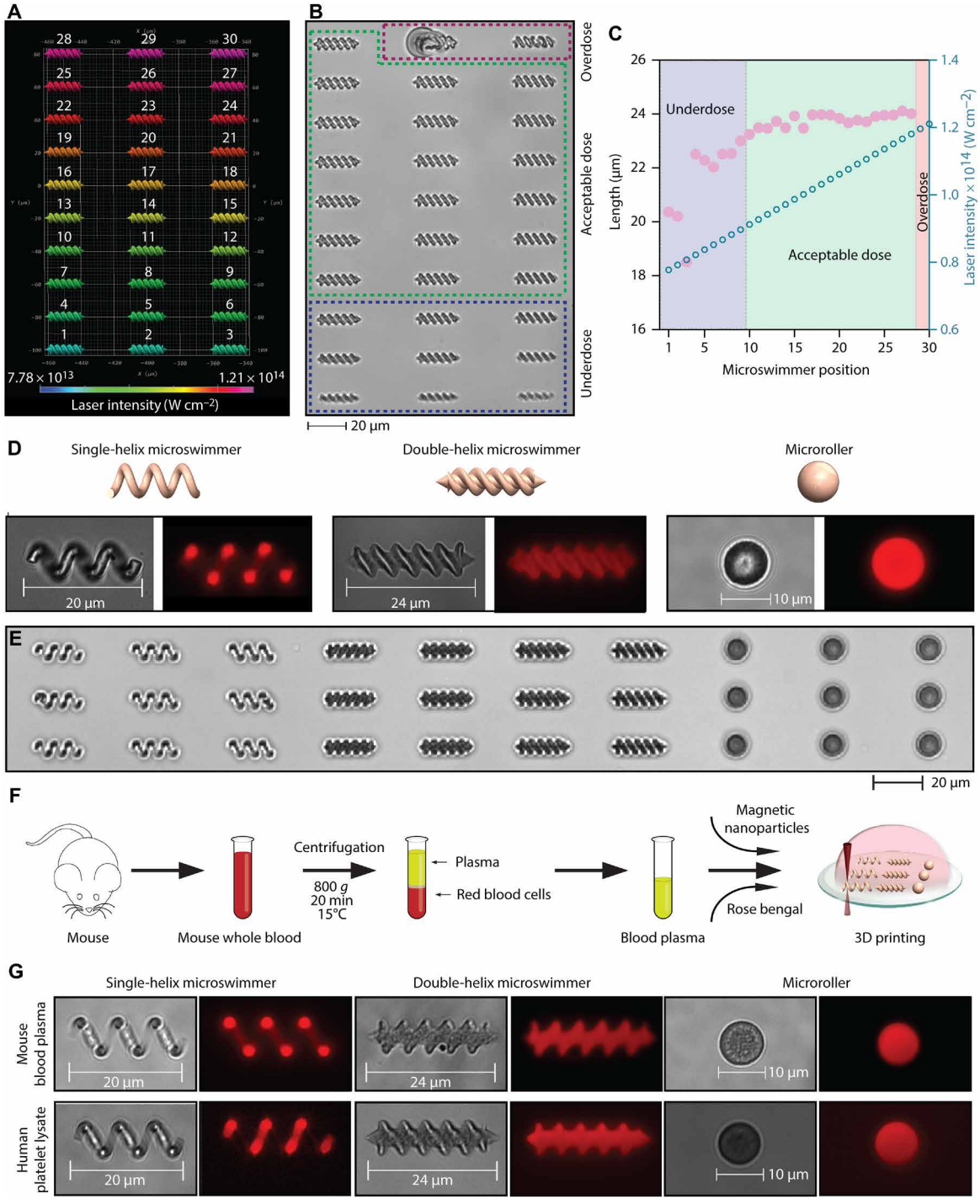

Fig. 2. 3D printed micromachines from bovine serum albumin, mouse blood plasma, and human platelet lysate. (**A**) A color-coded assignment of the systematically varied laser intensities for the fabrication of albumin microswimmer. (**B**) The structural quality of the 3D printed albumin microswimmers assessed with differential interference contrast (DIC) imaging. (**C**) The length of the microswimmers measured as a function of the applied laser intensity. (**D** and **E**) DIC and fluorescence images of the 3D printed albumin-based micromachines. (**F**) Fabrication strategy of the mouse plasma micromachines. (**G**) DIC and fluorescence images of the 3D printed plasma and platelet lysate microswimmers.

solid structural defects due to the local heating-based bubble formations. Therefore, we fabricated the albumin micromachines at an optimum laser intensity with high structural fidelity and dimensions (a maximum 2.5% margin of error was considered acceptable). In Fig. 2 (D and E), we demonstrate the optimized printing of magnetic single- and double-helix microswimmers and microrollers from albumin. Since the photoinitiator rose bengal has natural autofluorescence (excitation/emission: 560/570 nm), it was possible to

Downloaded from https://www.science.org on November 24, 2021

visualize the micromachines under fluorescence microscopy. As highlighted above, albumin is found in the blood plasma in sufficiently high amounts to realize a personalized albumin micromachine approach. One microliter of whole blood roughly yields 50 mg of albumin. Given that ca. 29 wt % albumin corresponds to the minimum monomer concentration that allows 3D printing with two-photon polymerization, this amount can be used to prepare around 150 μl of precursor solution for 3D printing. With a typical 10 μl of precursor solution in the fabrication channel, our 3D printing capability can produce at least 200,000 micromachines on a 1-cm^2 glass substrate. A back-of-the-envelope calculation then estimates that it is possible to fabricate more than 30,000,000 albumin micromachines from 1 ml of whole blood using our existing straightforward sample preparation and handling tools.

Next, we demonstrated the printing of micromachines from raw blood plasma and platelet lysate. We isolated fresh blood plasma from pooled C57BL/6 mice whole blood with density gradient centrifugation (Fig. 2F). In Fig. 2G and fig. S2, we showed the micromachines with optimized printing parameters from mouse blood plasma and human platelet lysate. We printed the raw mouse blood plasma as is, without concentrating it. This result suggests the involvement of other proteinaceous biomacromolecules, such as globulins and fibrinogen, in addition to albumin to ensure adequate monomer concentrations for successful high-fidelity printing to be achieved.

Magnetic actuation and steering of the micromachines

We applied rotational magnetic fields with a custom-designed Helmholtz coil electromagnetic system mounted on an inverted microscope, as we previously demonstrated (*39*). The rotational magnetic fields actuated and steered the micromachines by exerting torque in the direction perpendicular to their rotational axis (Fig. 3, A to C, and movies S1 to S3)

$$\vec{\tau}_m = V(\vec{M}x\vec{B})$$

where $\vec{\tau}_m$ is the magnetic torque, V is the volume of the magnetic component, $\vec{M}$ is the magnetization vector, and $\vec{B}$ is the applied magnetic field (*40*). Single- and double-helix microswimmers convert the rotational motion to translational motion due to their asymmetric body shape (*41*). Microrollers convert the rotation into directional mobility through nonslip contact with the surface (*42*). We increased the actuation frequency stepwise to determine the step-out frequencies where the micromachines are no longer able to overcome the resistive torque exerted by the fluid. We measured their maximum forward velocities at the step-out frequencies as 9.8, 9.1, and 9.3 μm s^{-1} for single-helix, double-helix, and microroller designs, respectively.

The velocity and the step-out frequency of the micromachines scale linearly with the volume of the magnetic component (*40*). Therefore, maximizing the total amount of magnetic nanoparticles loaded in the micromachines is essential for fast locomotion. We aimed to maximize the volume fraction of the magnetic nanoparticles in the precursor suspension during the 3D printing step. However, beyond a magnetic nanoparticle concentration of 20 mg ml^{-1}, the tendency for nanoparticle aggregation restricted the microfabrication process, as we and others observed previously (*20*, *39*, *43*). This problem can be circumvented in two ways. First, iron oxide nanoparticles with better colloidal stability can increase the magnetic volume. Second, stronger and biocompatible magnetic nanoparticle types, such as iron platinum, could substantially increase the magnitude of magnetization, as have been recently demonstrated (*44*, *45*).

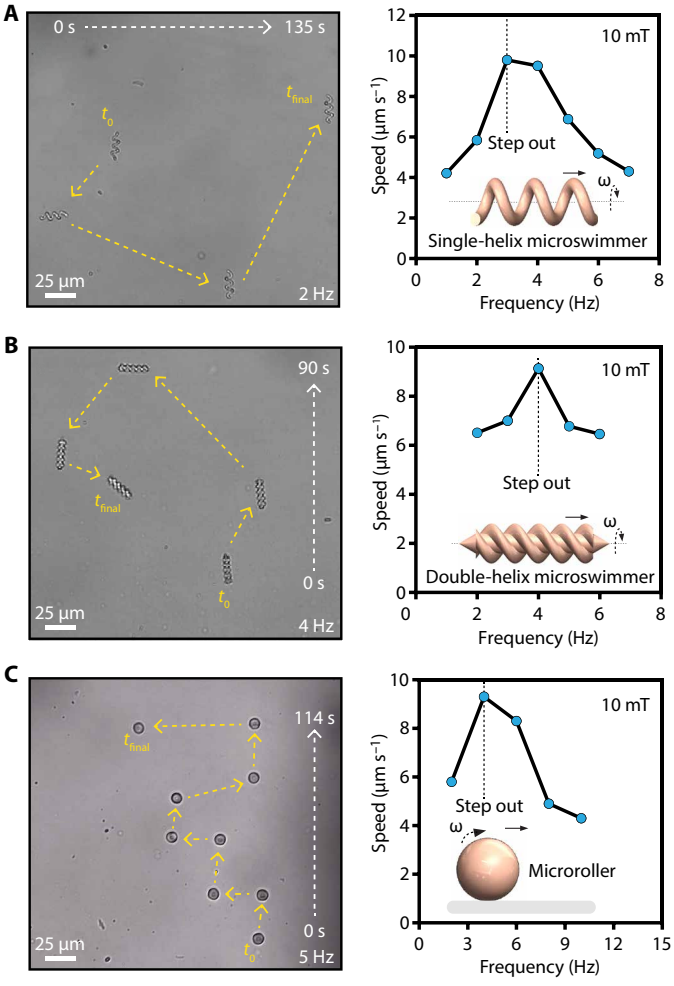

Fig. 3. Magnetic torque–based actuation and steering of the micromachines. Swimming trajectories and step-out frequencies of albumin microswimmers with varying designs: (**A**) A single-helix microswimmer, (**B**) double-helix microswimmer, and (**C**) microroller. The step-out frequencies are determined by stepwise increasing the actuation frequency.

Enzymatic degradability of the micromachines

Biodegradability is an essential aspect of the long-term biocompatibility of medical micromachines. Once the given tasks of a medical micromachine are accomplished, they should be retrieved or dissolved into nontoxic soluble products. The extended presence of nondegradable micromachines in the body could result in chronic inflammation (*3*). We used trypsin as a model protease to test the enzymatic degradability of the micromachines. Trypsin hydrolyses the peptide bonds in which the carbonyl group is formed either by an arginine or lysine residue, breaking down proteins into peptides and amino acids. It is found in the pancreatic juice at a concentration of 0.02 to 1 mg ml^{-1} (*46*). Here, we explored the degradability of the microswimmers by sweeping the trypsin concentration in the range of 0.1 to 2.5 mg ml^{-1} (fig. S3). At an unrealistically high

Downloaded from https://www.science.org on November 24, 2021

trypsin concentration, 2.5 mg ml^{-1}, we observed that the microswimmers were entirely degraded within 20 min at 37°C. The total degradation time was a function of the initial enzyme concentration. At more realistic high trypsin concentrations, such as 1 mg ml^{-1}, it took around 30 min for complete degradation and 60 min at 0.1 mg ml^{-1} (Fig. 4, A and B).

We measured the length and diameter of the microswimmers in the course of their enzymatic degradation process to understand the degradation mechanism. We observed that the albumin microswimmers started with rapid swelling followed by the complete collapse of their hydrogel network across all trypsin concentrations (Fig. 4B and movie S4). The initial swelling of the microswimmers indicates that trypsin enzymes could diffuse into the microswimmers and started the hydrolysis of the polymer chains uniformly across the microswimmer body. In the swelling phase, the water molecules enlarged pores that diffused into the polymer network faster than the hydrolysis of the polymer chains near the microswimmer surface. This relationship suggests that the observed phenomenon is bulk erosion (*47*). In bulk erosion, water continues to diffuse until it saturates the entire network. As the rate of water diffusion exceeds the rate of the bond cleavage reaction, uniform swelling continues until the collapse of the network becomes visible under the microscope.

The proteolytic degradation of albumin and plasma with trypsin was evident, whereas the microswimmers fabricated from platelet lysates were only partially degraded with trypsin (fig. S4). Alternatively, we used matrix metalloproteinase-2 and accutase, a mixture of protease and collagenases, with little change in the resulting degradation profile. These results suggest that the platelet lysate composition may contain other biomacromolecules in high amounts, such as large sugar or fat molecules, limiting the proteolytic degradation. Together, the degradation kinetics of the microswimmers made from different biomaterials should be more closely investigated for a targeted future application by considering all the pathophysiologically relevant tissue-specific proteases and other local conditions.

Cytotoxicity assessment

We assessed the biocompatibility by exposing cells to the intact albumin microswimmers and their enzymatic degradation products. First, we allowed mouse peritoneal macrophage cells, J774A.1, to interact with the intact albumin microswimmers for up to 48 hours. These macrophages did not exhibit a toxicity-stemmed behavioral change, as evidenced by the comparable viability and morphological features of normal healthy cells (fig. S5). Then, we exposed the degradation products from 1080 albumin microswimmers to primary human adipose–derived mesenchymal stem cells (haMSCs), which are exceptionally sensitive to toxic microenvironments compared to immortalized fibroblast cell lines (*48*). The cytotoxicity analyses based on the cellular membrane integrity and metabolic activity indicate that these sensitive stem cells did not show an acute toxic response (Fig. 4, C and D).

pH-responsive shape memory behavior

Proteins contain many amino and carboxylic acid groups, which dynamically change the protonation state with the environmental pH. Therefore, the proteinaceous micromachines can morph their

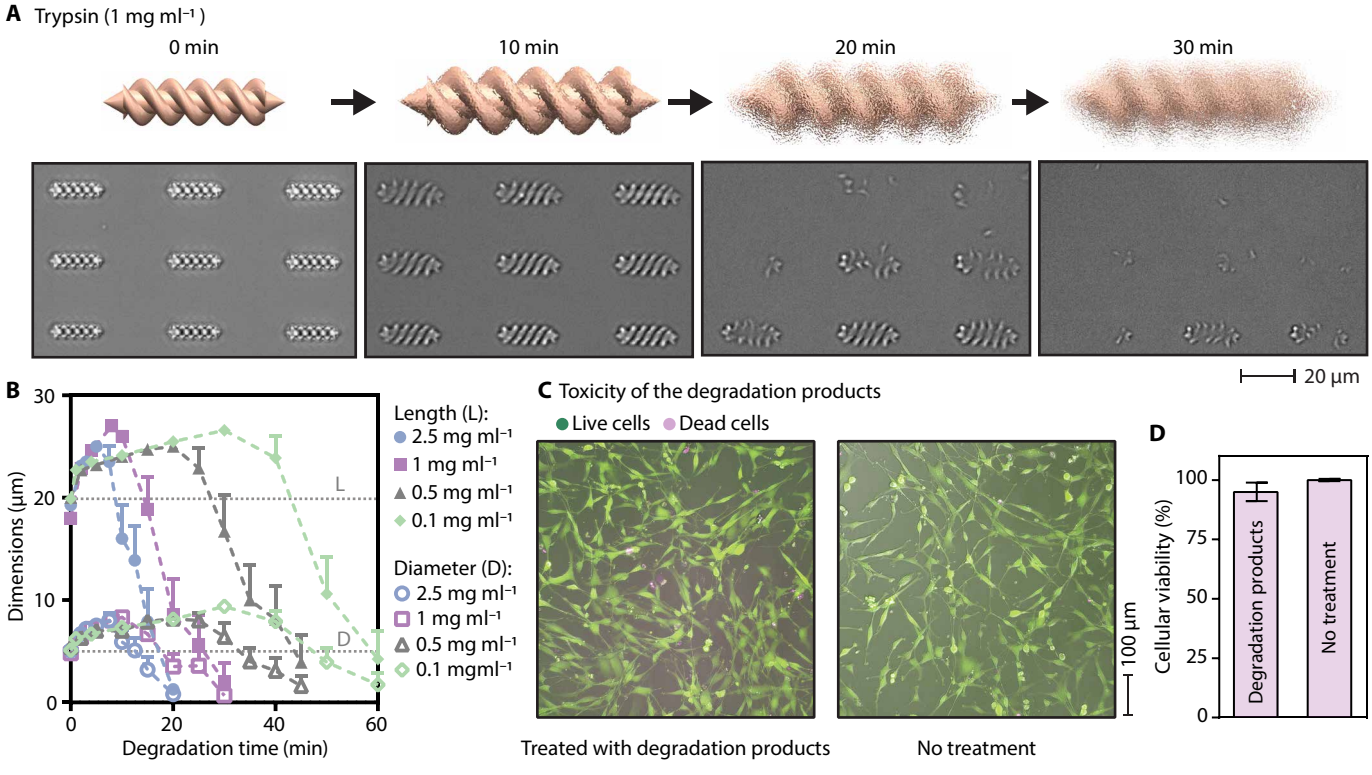

Fig. 4. Enzymatic degradation of the albumin microswimmers. (**A**) Enzymatic degradation observed under the time-lapse DIC imaging in the presence of trypsin enzyme at a concentration comparable to the pancreatic juice at 37°C. (**B**) An increase in the dimensions of albumin microswimmers during the degradation before the total collapse of the microswimmer fabric. (**C** and **D**) The biocompatibility of the degradation products of albumin microswimmers assessed by the viability of the exposed haMSCs at 24 hours. (C) Representative calcein acetoxymethyl ester/ethidium homodimer-1–stained fluorescence images of the exposed haMSCs. (D) The viability of the exposed haMSCs assessed based on the quantified intracellular adenosine 5′-triphosphate amount.

Downloaded from https://www.science.org on November 24, 2021

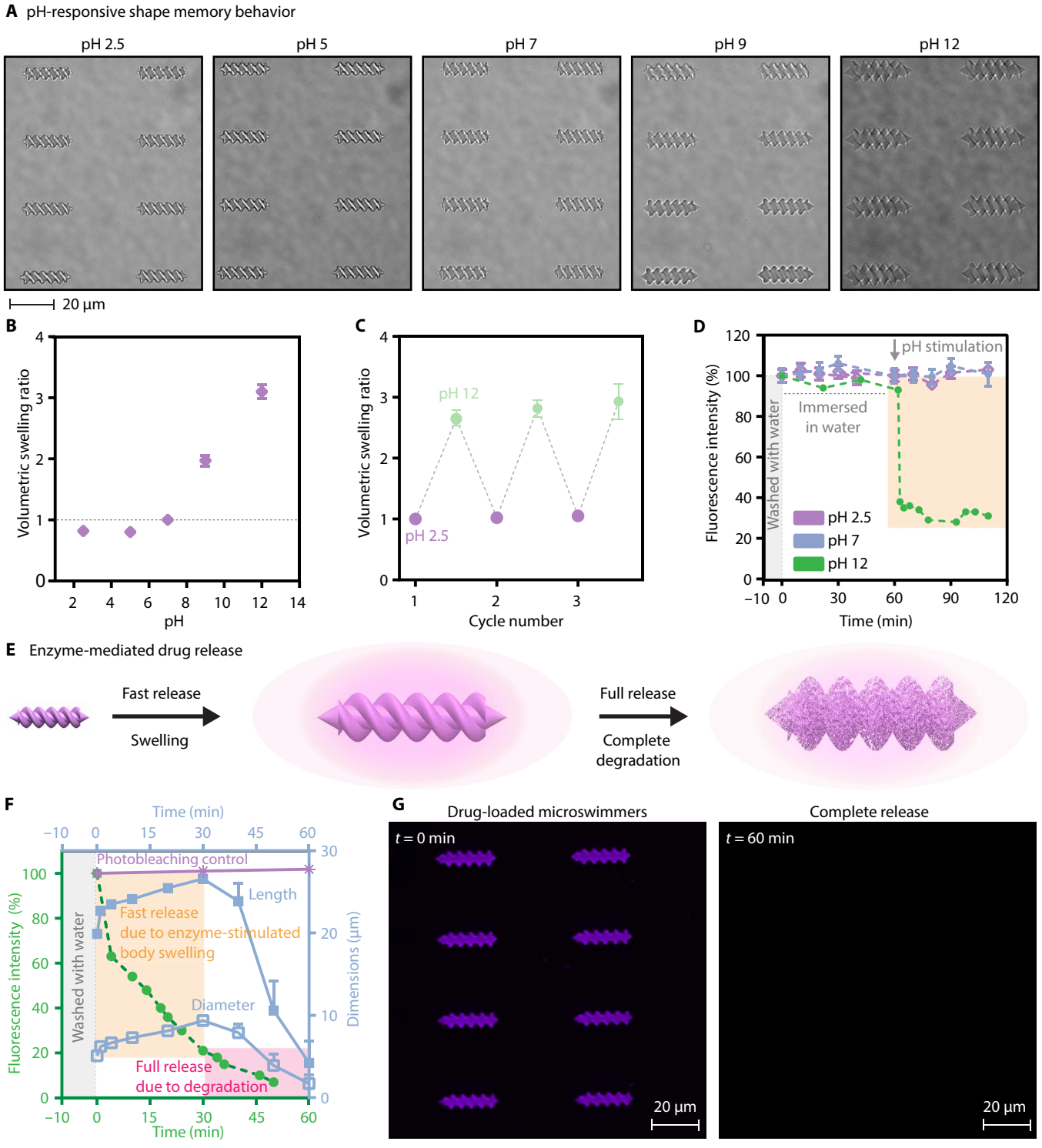

Fig. 5. Stimuli-responsive shape memory albumin microswimmers. (**A**) pH-responsive albumin microswimmers. (**B**) The volumetric swelling ratio of the microswimmers as a function of pH. The swelling ratios are normalized to the initial volume at pH 7. (**C**) Two-way shape memory behavior of the microswimmers in response to pH change. (**D**) pH-stimulated, body swelling–driven drug release from the albumin microswimmers. (**E**) Trypsin-stimulated two-step drug release dynamics from the microswimmers. (**F**) Trypsin-mediated cargo release kinetics at pH 7. (**G**) Representative fluorescence images of the drug-loaded microswimmers demonstrating the complete drug release with enzymatic degradation.

Downloaded from https://www.science.org on November 24, 2021

shapes in response to pH stimulus. To explore this, we investigated albumin and platelet lysate microswimmers in the pH range of 2.5 to 12 (Fig. 5A and fig. S6). Figure 5B shows the volumetric change of the albumin microswimmers in response to the pH change. They exhibited the lowest swelling ratio at pH 5, close to the isoelectric point of albumin (*49*). At pH 12, the deprotonated basic residues formed more robust bonds with water molecules, resulting in water absorption into the body and around a threefold volumetric increase (*28*). We obtained similar results for the platelet lysate microswimmers, showing a larger swelling ratio at pH 12, while the swelling ratio was less and comparable at acidic and neutral pH values (fig. S6).

We observed a shape memory behavior with the albumin microswimmers when the pH is reverted to the former state. We selected pH 2.5 and 12 end points for the cyclic reversibility because these pH values represent the two extreme cases of the swelling/shrinking capacity of the microswimmers. The microswimmers exhibited two-way shape memory behavior, demonstrating both the stability and robustness in responding to the extreme pH changes in the environment (Fig. 5C and fig. S7).

Stimuli-responsive cargo release

On-demand and on-target therapeutic release are some of the challenges in drug delivery applications of medical micromachines. Smart material systems exhibiting responsiveness to external triggers and environmental changes could open improved possibilities toward controlled cargo release. Here, because of their nanoporous hydrogel nature, pH, and enzymatic responsiveness, the proposed protein-based microswimmers might serve as environmentally responsive drug delivery and release platforms. As a showcase of this potential, we loaded a fluorescent small-molecule drug analog, CellTracker Deep Red Dye, into the porous network of the albumin microswimmers (fig. S8). We evaluated the release of this molecule by probing the fluorescence intensity in the microswimmer in response to pH change and enzymatic degradation in the given physiological microenvironment.

To understand the impact of the pH stimulus on the drug release, we first thoroughly washed the drug-loaded microswimmers followed by an hour of monitoring under ultrapure water at pH 7 to eliminate the contribution from the unstimulated diffusion (Fig. 5D). Then, we introduced the pH 2.5, 7, and 12 buffer solutions to the drug-loaded microswimmers. At pH 12, we observed a rapid decrease in the microswimmer fluorescent intensity, evidencing the outflux of the drug molecules. The rapid swelling of the microswimmers served as a switch for accelerated drug release. As they swelled, their hydrogel mesh size increased, and the entrapped drug was released. On the other hand, we did not observe a significant release from the microswimmers stimulated with pH 2.5 and 7 buffer solutions, because, at these pH values, no swelling was observed (Fig. 5B). The release at pH 12 reached a plateau, where ca. 30% of the drug remained inside the hydrogel network. The uncompleted release could be attributable to the physical interactions between the hydrogel network and the drug molecules.

The inherent responsiveness of the albumin microswimmers to enzymatic degradation could define an alternative stimuli-responsive drug release capability. When we treated the drug-loaded microswimmers with the trypsin enzyme, we observed the rapid swelling of the microswimmers, accompanied by the simultaneous release of the payloads into the environment (Fig. 5, E to F). Apart from pH-stimulated release, where the physisorption limits the bioavailability, the enzymatic degradation ensured the complete release of the drug molecules (Fig. 5, F and G, and fig. S9). These micromachines can carry drugs, cells, radio-labeled agents, and remote heating–based tumor therapy to the site of action with microscopic precision. We demonstrate that patient-derivable biomaterial-based micromachines can act smartly to the external pH and trypsin protease. Therefore, these micromachines can play an enabling role in a physiological environment where proteases play an enabling role during malignant progression, including tumor angiogenesis, invasion, and metastasis (*50*).

In summary, we demonstrated the potential of patient-derivable biomaterials as previously unidentified robotic materials. Their inherent responsiveness to pH and proteases can tailor personalized micromachines according to the specific biomedical application–based design requirements. Although the present study focused on the monolithic fabrication of micromachines from individual blood-harvested biomaterials, components of micromachines can also be assembled with a modular approach using various biomaterials to increase the functional complexity. Personalized robotic materials can potentially affect the design of various medical robots and devices toward substantially improved biocompatibility.

Nevertheless, with the degradation of the patient-specific dispersion matrix, other components can potentially pose safety risks. For example, in the present study, we used iron oxide nanoparticles as the magnetic transducers of the micromachines. The use of iron oxide nanoparticles was approved for intravenous administration in the United States and the European Union to treat iron deficiency anemia in adult patients with chronic kidney disease (*51*). As a result, it demonstrates an acceptable level of safety for these nanoparticles. However, like any other synthetic material, these nanoparticles can also result in adverse interactions (*52*). Therefore, this study aims to maximize biocompatibility while acknowledging the challenges of entirely evading the immune system's surveillance due to its additional synthetic components and potential morphological features (*13*) that may trigger immune cell response. In addition, when a micromachine is inside the body, many biomacromolecules, e.g., lipids and proteins, in the environment will interact with its surface to form an adsorption layer called protein corona (*3*, *53*). We previously showed that the phagocytic interactions with macrophages are markedly affected by the presence of the protein corona (*13*). Therefore, elucidating the formation of protein corona on the personalized micromachines and its impact on their safe functioning inside a specific pathophysiological context is essential.

MATERIALS AND METHODS

Preparation of albumin precursor mixture

An aqueous mixture was prepared containing bovine serum albumin (290 mg ml^{-1}; Sigma-Aldrich), 6.8 mM rose bengal (Sigma-Aldrich), iron oxide magnetic nanoparticles (20 mg ml^{-1}; 100-nm mean size; Chemicell), 80 mM NaCl (Sigma-Aldrich), 16 mM Hepes (Gibco), and 40 μl of dimethyl sulfoxide (Sigma-Aldrich) with rigorous vortex mixing and ultrasound sonication.

Preparation of platelet lysate precursor mixture

An aqueous mixture was prepared containing human platelet lysate (STEMCELL Technologies), rose bengal (20 mg ml^{-1}), and iron oxide magnetic nanoparticles (20 mg ml^{-1}) with rigorous vortex mixing and ultrasound sonication.

Downloaded from https://www.science.org on November 24, 2021

Preparation of blood plasma precursor mixture

Whole blood of freshly sacrificed C57BL/6 mouse was obtained from Einrichtung für Tierschutz, Tierärztlichen Dienst und Labortierkunde, Eberhard Karls Universität Tübingen and collected into EDTA-treated tubes. Plasma was separated from whole blood via centrifugation at 800*g* for 20 min at 15°C. The supernatant was denominated as plasma and directly transferred into a clean microcentrifuge tube. For the preparation of the precursor mixture, the plasma was mixed with rose bengal (20 mg ml^{-1}) and iron oxide magnetic nanoparticles (20 mg ml^{-1}) via vortex mixing and ultrasound sonication.

3D printing of the micromachines

3D printing of the micromachines was performed using a turn-the-key direct laser writing system (Photonic Professional, Nanoscribe GmbH, Germany) equipped with piezo scanners and galvanometric mirrors for high precision and microfabrication speed. A 63× oil-immersion objective (numerical aperture, 1.4) was used to achieve submicron size features. After the printing, the micromachines were developed with ultrapure water, and they were stored at 4°C underwater until further use. The polymerization of precursor solutions was performed in a closed channel to minimize solvent evaporation. During the 3D printing, we applied a uniform magnetic field in the direction normal to the rotation axes of the micromachines (Fig. 1). This uniform field helped form self-assembled chains of magnetic iron oxide nanoparticles to increase the micromachines' net magnetization, hence the applied torque for magnetic actuation (*39*).

Magnetic actuation

Micromachines were actuated and steered using our custom-built five-coiled electromagnetic setup mounted on an inverted microscope (Zeiss Axio Observer A1), as previously described (*39*). Horizontal pairs of the coil sets were calibrated to generate homogeneous field lines, i.e., without gradient, so that they would act like Helmholtz coils. The step-out frequencies of the micromachines were determined by gradually increasing the frequency of the magnetic field. The instantaneous velocities were calculated using an in-house open-access MATLAB code.

Enzymatic degradation assay

The degradation of microswimmers was assessed with trypsin enzyme (Gibco) by acquiring time-lapse differential interference contrast (DIC) images under a Nikon Eclipse Ti-E inverted microscope equipped with an environmental chamber to maintain the temperature at 37°C.

Cell culture and cytotoxicity assays

haMSCs (Cellular Engineering Technologies) were cultured in RPMI 1640 medium (Gibco) supplemented with 10% fetal bovine serum (FBS) (Gibco) and 1% penicillin/streptomycin (Gibco) in a humidified, 37°C and 5% CO_2 environment using 75-cm^2 polystyrene cell culture flasks. Cells were used at passage numbers lower than 10, and surface detachment during splitting was performed using trypsin (0.25 wt %)/EDTA solution when they reached 70% confluence.

Mouse peritoneal macrophage cells, J774A.1 (American Type Culture Collection), were cultured in Dulbecco's modified Eagle's medium (DMEM) supplemented with 10% FBS (Gibco) and 1% penicillin/streptomycin (Gibco) in a humidified, 37°C and 5% CO_2 environment using 75-cm^2 polystyrene cell culture flasks. Cells were used at passage numbers lower than 10, and surface detachment during splitting was performed using a cell scraper when they reached 80% confluence.

For the cytotoxicity experiments, J774A.1 cells were allowed to sediment on albumin microswimmers at a density of 2.8×10^4 cells cm^{-2}. At the end of 24 hours, the cells were treated with LIVE/DEAD cell imaging solution (Invitrogen), as described by the supplier. Live and dead cells were captured using the Nikon fluorescent microscope. The images were collected randomly from multiple sample locations to count live and dead cells using open-source image processing Fiji software.

To evaluate the toxicity of the degradation products, haMSCs were first seeded at a density of 3.1×10^4 cells cm^{-2} into surface-treated clear bottom black 96-well plates (Corning). After an overnight incubation following the seeding, haMSCs were exposed to the degradation products of 1080 albumin microswimmers for another 24 hours. Last, the cells were treated with CellTiter-Glo reagent, as described by the supplier (Promega), and the luminescence of the cell lysates was measured using a plate reader (BioTek's Synergy 2, Winooski, VT, USA). A parallel set of haMSCs was stained with live/dead cell imaging solution (Invitrogen) at the end of 24 hours for visual evidence.

pH responsiveness testing

pH buffer solutions were prepared as shown in table S2 for various pH values. Each 3D printed microswimmer array on the glass substrates was independently treated with the designated buffer solution until the equilibration was reached (ca. 5 min). The pH response was linked to the change in the length and diameter of the microswimmers, which were measured using the Nikon inverted microscope and analyzed using the Nikon NIS-Elements Advanced Research image analysis software from their raw microscopy images.

Two-way shape memory microswimmer testing

Cyclic swelling-shrinking behavior was performed by immersing microswimmers in pH 2.5 and 12 buffer solutions in a cyclic order. The equilibration was ensured within 5 min at each cycle of pH alteration.

pH-responsive drug release

Albumin microswimmers printed on a glass surface were loaded with a drug analog, CellTracker Deep Red Dye, with a molecular mass of 698.3 Da (Invitrogen). The microswimmers were immersed in 1 mM CellTracker Deep Red Dye solution overnight at 4°C. The microswimmers were equilibrated to room temperate and washed with a copious amount of water for 10 min before the drug release measurements. To assess the release, independent drug-loaded microswimmer arrays were stimulated with pH 2.5, 7, or 12 buffer solutions. Fluorescence intensities (bandpass emission: 670 nm) over 12 microswimmers in each group were measured using the Nikon software. Background fluorescence was subtracted from the measured values.

Enzyme-responsive drug release

CellTracker Deep Red Dye–loaded albumin microswimmers were immersed in trypsin solution (0.1 mg ml^{-1}) at 37°C under the Nikon inverted microscope. Fluorescence intensities (bandpass emission: 670 nm) over 12 microswimmers in each group were measured using the Nikon software. Background fluorescence was subtracted

Downloaded from https://www.science.org on November 24, 2021

from the measured values. A separate array of drug analog–loaded albumin microswimmers immersed in the ultrapure water was exposed to the excitation light source with the same intensity and exposure time to eliminate the drug release due to the photobleaching effect.

SUPPLEMENTARY MATERIALS

Supplementary material for this article is available at https://science.org/doi/10.1126/sciadv.abh0273

REFERENCES AND NOTES

1. M. Sitti, H. Ceylan, W. Hu, J. Giltinan, M. Turan, S. Yim, E. Diller, Biomedical applications of untethered mobile milli/microrobots. *Proc. IEEE Inst. Electr. Electron. Eng.* **103**, 205–224 (2015).
2. H. Ceylan, J. Giltinan, K. Kozielski, M. Sitti, Mobile microrobots for bioengineering applications. *Lab Chip* **17**, 1705–1724 (2017).
3. H. Ceylan, I. C. Yasa, K. Ugur, W. Hu, M. Sitti, Translational prospects of untethered medical microrobots. *Prog. Biomed. Eng.* **1**, 012002 (2019).
4. F. Soto, J. Wang, R. Ahmed, U. Demirci, Medical micro/nanorobots in precision medicine. *Adv. Sci.* **7**, 2002203 (2020).
5. C. C. J. Alcântara, F. C. Landers, S. Kim, C. De Marco, D. Ahmed, B. J. Nelson, S. Pané, Mechanically interlocked 3D multi-material micromachines. *Nat. Commun.* **11**, 5957 (2020).
6. D. Ahmed, A. Sukhov, D. Hauri, D. Rodrigue, G. Maranta, J. Harting, B. J. Nelson, Bioinspired acousto-magnetic microswarm robots with upstream motility. *Nat. Mach. Intell.* **3**, 116–124 (2021).
7. H. Ceylan, I. C. Yasa, M. Sitti, 3D chemical patterning of micromaterials for encoded functionality. *Adv. Mater.* **29**, 1605072 (2017).
8. J. Li, M. Pumera, 3D printing of functional microrobots. *Chem. Soc. Rev.* **50**, 2794–2838 (2021).
9. M. A. Rahman, J. Cheng, Z. Wang, A. T. Ohta, Cooperative micromanipulation using the independent actuation of fifty microrobots in parallel. *Sci. Rep.* **7**, 3278 (2017).
10. H. Xie, M. Sun, X. Fan, Z. Lin, W. Chen, L. Wang, L. Dong, Q. He, Reconfigurable magnetic microrobot swarm: Multimode transformation, locomotion, and manipulation. *Sci. Robot.* **4**, eaav8006 (2019).
11. D. F. Williams, Biocompatibility in clinical practice: Predictable and unpredictable outcomes. *Prog. Biomed. Eng.* **1**, 013001 (2019).
12. E. Blanco, H. Shen, M. Ferrari, Engineering nanoparticles to overcome immunological barriers for enhanced drug delivery. *Nat. Biotechnol.* **33**, 941–951 (2015).
13. I. C. Yasa, H. Ceylan, U. Bozuyuk, A. M. Wild, M. Sitti, Elucidating the interaction dynamics between microswimmer body and immune system for medical microrobots. *Sci. Robot.* **5**, eaaz3867 (2020).
14. S. D. Li, L. Huang, Nanoparticles evading the reticuloendothelial system: Role of the supported bilayer. *Biochim. Biophys. Acta* **1788**, 2259–2266 (2009).
15. M. D. McSweeney, Z. C. Versfeld, D. M. Carpenter, S. K. Lai, Physician awareness of immune responses to polyethylene glycol-drug conjugates. *Clin. Transl. Sci.* **11**, 162–165 (2018).
16. P. Cabanach, A. Pena-Francesch, D. Sheehan, U. Bozuyuk, O. Yasa, S. Borros, M. Sitti, Zwitterionic 3D-printed non-immunogenic stealth microrobots. *Adv. Mater.* **32**, e2003013 (2020).
17. B. Li, Z. Yuan, H. C. Hung, J. Ma, P. Jain, C. Tsao, J. Xie, P. Zhang, X. Lin, K. Wu, S. Jiang, Revealing the immunogenic risk of polymers. *Angew. Chem. Int. Ed. Engl.* **57**, 13873–13876 (2018).
18. N. Buss, O. Yasa, Y. Alapan, M. B. Akolpoglu, M. Sitti, Nanoerythrosome-functionalized biohybrid microswimmers. *APL Bioeng.* **4**, 026103 (2020).
19. J. Shintake, H. Sonar, E. Piskarev, J. Paik, D. Floreano, Soft pneumatic gelatin actuator for edible robotics, arXiv:1703.01423 (2017).
20. H. Ceylan, I. C. Yasa, O. Yasa, A. F. Tabak, J. Giltinan, M. Sitti, 3D-printed biodegradable microswimmer for theranostic cargo delivery and release. *ACS Nano* **13**, 3353–3362 (2019).
21. S. R. Goudu, I. C. Yasa, X. H. Hu, H. Ceylan, W. Q. Hu, M. Sitti, Biodegradable untethered magnetic hydrogel milli-grippers. *Adv. Funct. Mater.* **30**, 2004975 (2020).
22. F. DeLustro, J. Dasch, J. Keefe, L. Ellingsworth, Immune responses to allogeneic and xenogeneic implants of collagen and collagen derivatives. *Clin. Orthop. Relat. Res.* **260**, 263–279 (1990).
23. H. Lu, T. Hoshiba, N. Kawazoe, G. Chen, Autologous extracellular matrix scaffolds for tissue engineering. *Biomaterials* **32**, 2489–2499 (2011).
24. R. F. Reiss, M. C. Oz, Autologous fibrin glue: Production and clinical use. *Transfus. Med. Rev.* **10**, 85–92 (1996).
25. S. C. Santos, C. A. Custodio, J. F. Mano, Photopolymerizable platelet lysate hydrogels for customizable 3D cell culture platforms. *Adv. Healthc. Mater.* **7**, e1800849 (2018).
26. A. Selimis, V. Mironov, M. Farsari, Direct laser writing: Principles and materials for scaffold 3D printing. *Microelectron. Eng.* **132**, 83–89 (2015).
27. X. Hu, I. C. Yasa, Z. Ren, S. R. Goudu, H. Ceylan, W. Hu, M. Sitti, Magnetic soft micromachines made of linked microactuator networks. *Sci. Adv.* **7**, eabe8436 (2021).
28. S. Wei, J. Liu, Y. Zhao, T. Zhang, M. Zheng, F. Jin, X. Dong, J. Xing, X. Duan, Protein-based 3D microstructures with controllable morphology and pH-responsive properties. *ACS Appl. Mater. Interfaces* **9**, 42247–42257 (2017).
29. E. I. Alarcon, H. Poblete, H. Roh, J.-F. Couture, J. Comer, I. E. Kochevar, Rose bengal binding to collagen and tissue photobonding. *ACS Omega* **2**, 6646–6657 (2017).
30. C. M. Wertheimer, C. Elhardt, S. M. Kaminsky, L. Pham, Q. Pei, B. Mendes, S. Afshar, I. E. Kochevar, Enhancing rose bengal-photosensitized protein crosslinking in the cornea. *Invest. Ophthalmol. Vis. Sci.* **60**, 1845–1852 (2019).
31. A. Spencer, P. Gazzani, D. A. Thompson, Acrylate and methacrylate contact allergy and allergic contact disease: A 13-year review. *Contact Derm.* **75**, 157–164 (2016).
32. S. Tsao, M. Yao, H. Tsao, F. P. Henry, Y. Zhao, J. J. Kochevar, R. W. Redmond, I. E. Kochevar, Light-activated tissue bonding for excisional wound closure: A split-lesion clinical trial. *Br. J. Dermatol.* **166**, 555–563 (2012).
33. N. Vanerio, M. Stijnen, B. de Mol, L. M. Kock, Biomedical applications of photo- and sono-activated rose bengal: A review. *Photobiomodul. Photomed. Laser. Surg.* **37**, 383–394 (2019).
34. M. A. Zeeshan, R. Grisch, E. Pellicer, K. M. Sivaraman, K. E. Peyer, J. Sort, B. Ozkale, M. S. Sakar, B. J. Nelson, S. Pane, Hybrid helical magnetic microrobots obtained by 3D template-assisted electrodeposition. *Small* **10**, 1284–1288 (2014).
35. S. Gervasoni, A. Terzopoulou, C. Franco, A. Veciana, N. Pedrini, J. T. Burri, C. de Marco, E. C. Siringil, X.-Z. Chen, B. J. Nelson, J. Puigmartí-Luis, S. Pané, CANDYBOTS: A new generation of 3D-printed sugar-based transient small-scale robots. *Adv. Mater.* **32**, e2005652 (2020).
36. U. Bozuyuk, O. Yasa, I. C. Yasa, H. Ceylan, S. Kizilel, M. Sitti, Light-triggered drug release from 3D-printed magnetic chitosan microswimmers. *ACS Nano* **12**, 9617–9625 (2018).
37. Y. Alapan, U. Bozuyuk, P. Erkoc, A. C. Karacakol, M. Sitti, Multifunctional surface microrollers for targeted cargo delivery in physiological blood flow. *Sci. Robot.* **5**, eaba5726 (2020).
38. Y.-W. Lee, H. Ceylan, I. C. Yasa, U. Kilic, M. Sitti, 3D-printed multi-stimuli-responsive mobile micromachines. *ACS Appl. Mater. Interfaces* **13**, 12759–12766 (2021).
39. I. C. Yasa, A. F. Tabak, O. Yasa, H. Ceylan, M. Sitti, 3D-printed microrobotic transporters with recapitulated stem cell niche for programmable and active cell delivery. *Adv. Funct. Mater.* **29**, 1808992 (2019).
40. M. Sitti, *Mobile Microrobotics* (MIT Press, 2017).
41. E. M. Purcell, Life at low Reynolds number. *Am. J. Phys.* **45**, 3–11 (1977).
42. A. Kaiser, A. Snezhko, I. S. Aranson, Flocking ferromagnetic colloids. *Sci. Adv.* **3**, e1601469 (2017).
43. C. Peters, V. Costanza, S. Pané, B. J. Nelson, C. Hierold, "Superparamagnetic hydrogels for two-photon polymerization and their application for the fabrication of swimming microrobots," in Proceedings *18th International Conference on Solid-State Sensors, Actuators and Microsystems* (*TRANSDUCERS 2015*) (IEEE, 2015), pp. 764–767.
44. V. M. Kadiri, C. Bussi, A. W. Holle, K. Son, H. Kwon, G. Schutz, M. G. Gutierrez, P. Fischer, Biocompatible magnetic micro- and nanodevices: Fabrication of FePt nanopropellers and cell transfection. *Adv. Mater.* **32**, e2001114 (2020).
45. J. Giltinan, V. Sridhar, U. Bozuyuk, D. Sheehan, M. Sitti, 3D microprinting of iron platinum nanoparticle-based magnetic mobile microrobots. *Adv. Intell. Syst.* **3**, 2000204 (2021).
46. W. Kong, K. M. Conalogue, L. M. Khitin, M. D. Hollenberg, D. G. Payan, S. K. Böhm, N. W. Bunnett, Luminal trypsin may regulate enterocytes through proteinase-activated receptor 2. *Proc. Natl. Acad. Sci. U.S.A.* **94**, 8884–8889 (1997).
47. B. Laycock, M. Nikolić, J. M. Colwell, E. Gauthier, P. Halley, S. Bottle, G. George, Lifetime prediction of biodegradable polymers. *Prog. Polym. Sci.* **71**, 144–189 (2017).
48. M. Scanu, L. Mancuso, G. Cao, Evaluation of the use of human mesenchymal stem cells for acute toxicity tests. *Toxicol. In Vitro* **25**, 1989–1995 (2011).
49. K. Baler, O. A. Martin, M. A. Carignano, G. A. Ameer, J. A. Vila, I. Szleifer, Electrostatic unfolding and interactions of albumin driven by pH changes: A molecular dynamics study. *J. Phys. Chem. B* **118**, 921–930 (2014).
50. S. D. Mason, J. A. Joyce, Proteolytic networks in cancer. *Trends Cell Biol.* **21**, 228–237 (2011).
51. R. Provenzano, B. Schiller, M. Rao, D. Coyne, L. Brenner, B. J. G. Pereira, Ferumoxytol as an intravenous iron replacement therapy in hemodialysis patients. *Clin. J. Am. Soc. Nephrol.* **4**, 386–393 (2009).
52. D. Rampton, J. Folkersen, S. Fishbane, M. Hedenus, S. Howaldt, F. Locatelli, S. Patni, J. Szebeni, G. Weiss, Hypersensitivity reactions to intravenous iron: Guidance for risk minimization and management. *Haematologica* **99**, 1671–1676 (2014).
53. A. E. Nel, L. Mädler, D. Velegol, T. Xia, E. M. V. Hoek, P. Somasundaran, F. Klaessig, V. Castranova, M. Thompson, Understanding biophysicochemical interactions at the nano-bio interface. *Nat. Mater.* **8**, 543–557 (2009).

Acknowledgments

Funding: This work was funded by the Max Planck Society and European Research Council (ERC) Advanced Grant SoMMoR project (grant no. 834531). **Author contributions:** H.C., N.O.D., and M.S. proposed and designed the research. H.C., M.N.M., and Z.U.K. optimized the

Downloaded from https://www.science.org on November 24, 2021

microfabrication. H.C. and N.O.D. performed the bulk synthesis of the micromachines for characterization studies. N.O.D. performed magnetic actuation experiments. H.C. and N.O.D. performed and analyzed the enzymatic degradation and responsive drug release experiments. H.C., N.O.D., and I.C.Y. prepared the manuscript figures. H.C., N.O.D., and M.S. wrote the paper. All authors agreed on the final version of the initial submission and the revised version.
Competing interests: The authors declare that they have no competing interests. **Data and materials availability:** All data needed to evaluate the conclusions in the paper are present in the paper and/or the Supplementary Materials.

Submitted 10 February 2021
Accepted 14 July 2021
Published 3 September 2021
10.1126/sciadv.abh0273

Citation: H. Ceylan, N. O. Dogan, I. C. Yasa, M. N. Musaoglu, Z. U. Kulali, M. Sitti, 3D printed personalized magnetic micromachines from patient blood–derived biomaterials. *Sci. Adv.* **7**, eabh0273 (2021).

Downloaded from https://www.science.org on November 24, 2021

ScienceAdvances

3D printed personalized magnetic micromachines from patient blood–derived biomaterials

Hakan CeylanNihal Olcay DoganImmihan Ceren YasaMirac Nur MusaogluZeynep Umut KulaliMetin Sitti

Sci. Adv., 7 (36), eabh0273. • DOI: 10.1126/sciadv.abh0273

View the article online
https://www.science.org/doi/10.1126/sciadv.abh0273
Permissions
https://www.science.org/help/reprints-and-permissions

Downloaded from https://www.science.org on November 24, 2021

Use of think article is subject to the Terms of service

Science Advances (ISSN) is published by the American Association for the Advancement of Science. 1200 New York Avenue NW, Washington, DC 20005. The title *Science Advances* is a registered trademark of AAAS.
Copyright © 2021 The Authors, some rights reserved; exclusive licensee American Association for the Advancement of Science. No claim to original U.S. Government Works. Distributed under a Creative Commons Attribution License 4.0 (CC BY).